

1 Remote hydrological control on crustal seismicity

2 Francesco Pintori (Corresponding author, francesco.pintori@ingv.it)^{a,b}, Enrico Serpelloni
3 (enrico.serpelloni@ingv.it)^a, Laurent Longuevergne (laurent.longuevergne@univ-
4 rennes1.fr)^c, Alexander Garcia-Aristizabal (alexander.garcia@ingv.it)^a, Maria Elina
5 Belardinelli (mariaelina.belardinelli@unibo.it)^b, Licia Faenza (licia.faenza@ingv.it)^a, Lucio
6 D'Alberto (lucio.dalberto@arpa.veneto.it)^d, Adriano Gualandi
7 (adriano.geolandi@gmail.com)^{e,f}

8 ^a Istituto Nazionale di Geofisica e Vulcanologia, Italy.

9 ^b Università di Bologna, Dipartimento di Fisica e Astronomia, Settore di Geofisica, Bologna,
10 Italy.

11 ^c Geosciences Rennes, UMR CNRS 6118, Université de Rennes 1, Rennes, France.

12 ^d ARPA Veneto, Inland Waters Office, Padova, Italy.

13 ^e Department of Geological and Planetary Sciences, California Institute of Technology,
14 Pasadena, CA, USA.

15 ^f Jet Propulsion Laboratory, California Institute of Technology, Pasadena, CA, USA.

16

17

18 **Keywords:** GNSS; hydrology; non-tectonic deformation; stress changes; seismicity rates;

19 Alps

20

21 **Highlights:**

- 22 • Changes in terrestrial water storage modulate horizontal transient deformation
- 23 • Hydrologically-active fractures focus groundwater fluxes and pressure changes
- 24 • Pressure changes in shallow fractures cause large stress changes at seismogenic
25 depth
- 26 • Background seismicity rates are correlated with terrestrial water content

27

28 **Abstract**

29 It is known that changes in continental water storage can produce vertical surface
30 deformation, induce crustal stress perturbations and modulate seismicity rates. However, the
31 degree to which local changes in terrestrial water content influence the occurrence of
32 earthquakes remains an open problem. We show how changes in terrestrial water storage,
33 computed for a ~ 1000 km² basin, focus deformation in a narrow zone, causing horizontal,
34 non-seasonal displacements and modulating crustal seismicity rates. We present results
35 from a karstic mountain range located at the edge of the Adria-Eurasia plate boundary
36 system in northern Italy, where slow shortening rates (~ 1 mm/yr) are accommodated across
37 a complex fold-and-thrust belt. The presence of geological structures with high
38 permeabilities and of deeply rooted hydrologically-active fractures focus groundwater fluxes
39 and pressure changes, generating transient horizontal deformation and perturbations of
40 crustal stress up to 25 kPa at seismogenic depths. The background seismicity rates are
41 correlated, without evident temporal delay, with the terrestrial water content in the
42 hydrological basin. Being independent from hydraulic diffusivity, seismicity modulation is
43 likely affected by direct stress changes on faults planes.

44

45

46

47

48

49

50

51

52 **1. Introduction**

53 Constant redistribution of surface loads due to continental hydrology (van Dam et al., 2001)
54 causes measurable deformation of the Earth's surface. In particular, seasonal hydrological
55 mass movements turned out to influence tectonic deformation of the lithosphere and
56 modulate seismicity rates in several tectonic environments (Bettinelli et al., 2008; Craig et
57 al., 2017). While seasonal modulation of seismicity associated with vertical loading is a
58 known process (Bettinelli et al., 2008; Craig et al., 2017), other hydrologically-driven non-
59 seasonal deformation, mainly acting on the horizontal components, have been more recently
60 recognized in the peri-Adriatic region (Devoti et al., 2018; Silverii et al., 2016; Serpelloni et
61 al., 2018). Here, dense GNSS networks and important karst aquifers are present along the
62 seismically active Apennine and South Alpine mountain chains. The hydrological nature of
63 these deformation signals has been suggested based on temporal correlation between
64 geodetic displacements and precipitation or spring discharge data (Hainzl et al., 2006;
65 D'Agostino et al., 2018). Measurements of groundwater contents are not available because
66 of the lack of water wells in mountainous regions; however, the Gravity Recovery and
67 Climate Experiment (GRACE) can provide complementary independent observations of total
68 water mass, but with a coarse spatial resolution (greater than scales of 300 km; Famiglietti et
69 al., 2011). Changes in groundwater levels in karst aquifers, or fractures associated with karst
70 systems, are considered the most likely mechanisms to explain the observed deformation,
71 which is characterized by larger displacements in the horizontal components than in the
72 vertical one (Devoti et al., 2015; Serpelloni et al., 2018).

73 Identifying and extracting non-tectonic signals from geodetic measurements remains critical
74 to detect potential tectonic signals of small amplitude and to improve the accuracy and
75 precision of interseismic deformation estimates. Moreover, studying hydrological deformation
76 signals can provide new clues on elastic (Chanard et al., 2014; Drouin et al., 2016) and
77 viscoelastic (Chanard et al., 2018) properties of the Earth, on continental water storage
78 fluctuations (Borsa et al., 2014; Fu et al., 2013) and on the possible relationship between
79 hydrologically-driven stress changes and earthquake nucleation. Two mechanisms by which
80 hydrology can modulate earthquake occurrence have been suggested: variations in pore-

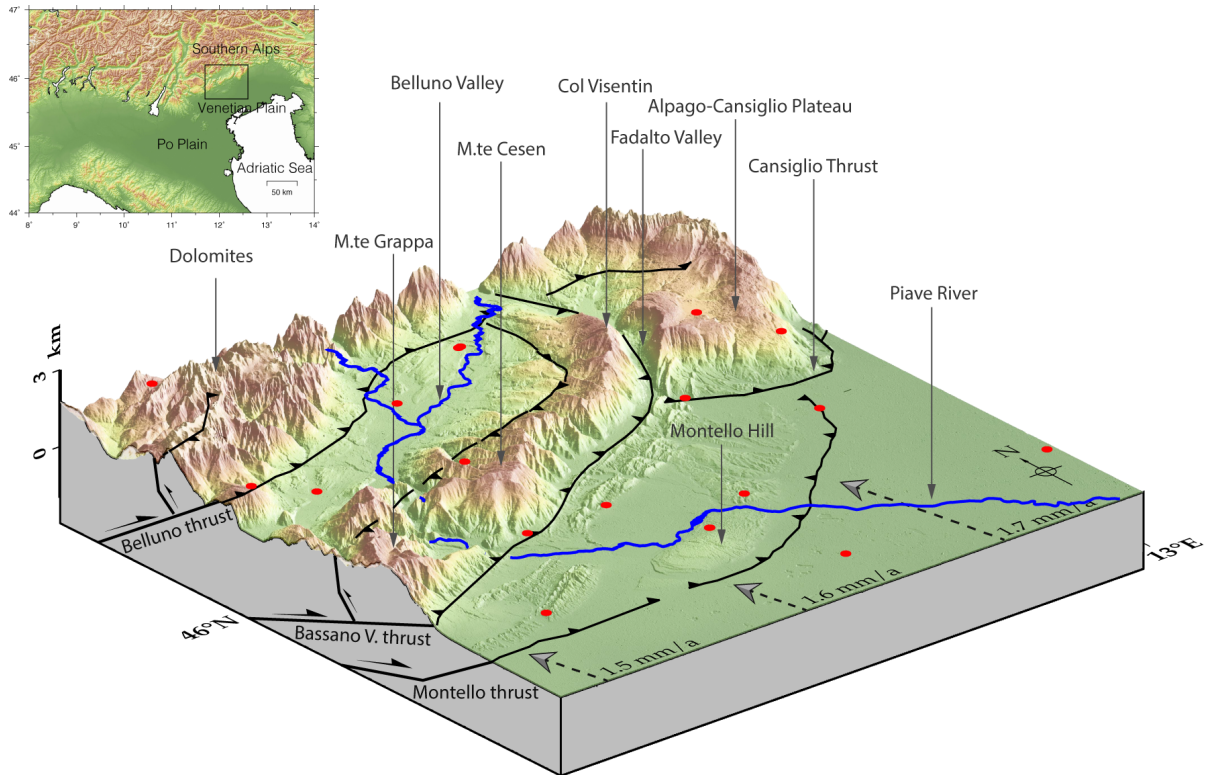
81 fluid pressure at hypocentral depths (Hainzl et al., 2006) and direct stress on the fault plane
82 (Bettinelli et al., 2008; Craig et al., 2017; Johnson et al., 2017; D'Agostino et al., 2018). An
83 effective way to discriminate between these two processes is the presence of a time lag
84 between hydrological indicators and seismicity rates. In fact, while the effect of the direct
85 stress can be considered instantaneous, hydraulic diffusivity at hypocentral depth determine
86 a time lag between hydrological and seismological indicators, if pore-fluid pressure variations
87 are the main driver of earthquake rates modulation.

88 In this work we study a segment of the Adria-Eurasia plate boundary in North-Eastern Italy
89 (Fig. 1), where ~70% of the plate convergence is presently accommodated across a south-
90 vering fold-and-thrust belt (Serpelloni et al., 2016; Anderlini et al., 2020). The main thrusts
91 are, from the internal parts to the foreland, the Valsugana thrust, the Belluno thrust and the
92 Bassano-Valdobbiadene thrust (BVT), the latter being associated with a morphological relief
93 of ~1200 m above the plain, known as Pedemountain flexure (Fig. 1). The southernmost
94 active front is now mainly buried beneath the alluvial deposits of the Venetian plain and
95 sealed by Late Miocene to Quaternary (~7–2.5 Ma) deposits (Fantoni et al., 2002),
96 consisting in the Montello thrust (Fantoni et al., 2002; Galadini et al., 2005). The Montello hill
97 (Fig. 1) is generally interpreted as an actively growing ramp anticline on top of the north
98 dipping thrust that has migrated south of the mountain into the foreland (Serpelloni et al.,
99 2016).

100 The main geomorphological feature of the area is the presence of the NE-SW oriented
101 Belluno Valley, where the Piave river flows, bounded to the north by the Dolomites and to the
102 south by the Monte Grappa massif, the Monte Cesen-Col Visentin (MCCV) mountain chain
103 and the Alpago-Cansiglio plateau (see Fig. 1). The MCCV is the morphological expression of
104 an anticline associated with the BVT and back-thrust system, and it is crossed by the Piave
105 river that flows to the southeast reaching the Montello hill. Highly productive fissured,
106 hydrologically independent, karst aquifers are present in the area (Fig. 3; Filippini et al.,
107 2018): in the Dolomites, one associated with the MCCV and one with the Alpago-Cansiglio
108 plateau.

109 We find a strong temporal correlation between groundwater level changes in the Belluno

110 Valley, estimated from hydrological modeling, geodetic transient horizontal displacements
111 and seismicity rates. We link hydrology to crustal deformation and geological structures by
112 adopting physically-based models constrained by precipitation, temperature and river flow
113 data and subsurface geological information; then, we show how water collected in a ~1000
114 km² basin focuses groundwater fluxes and pressure changes in a relatively narrow
115 geological structure, generating transient horizontal deformation and perturbations of crustal
116 stress of up to 25 kPa at seismogenic depths, modulating seismicity.



117

118

119 **Figure 1.** 3D view (from SW) of the study area. The dashed arrows indicate the Adria-
120 Eurasia convergence rate and direction, predicted from a GNSS-derived rotation pole
121 (Serpelloni et al., 2016). The digital elevation model, with topographic exaggeration, is
122 obtained from ALOS Global Digital Surface Model data. The black lines represent the major
123 fault lines. The red dots indicate the position of the GPS stations.

124

125

126

127

128 **2. GNSS data and time-series analysis**

129 Displacement time-series from GNSS stations in the 2010.0-2019.3 time span (Fig. 2 and
130 Supplementary Figure S1.1), obtained following the procedures described in the
131 Supplementary material (S1.1), have been analyzed with a blind source separation algorithm
132 based on variational Bayesian Independent Component Analysis (vbICA; Gualandi et al.,
133 2016). This approach, which uses a generative model to recreate the observations, allows
134 extracting the spatiotemporal information of independent sources of deformation without
135 imposing any specific spatial distribution or temporal function but extracting them directly
136 from the observations, and it has been successfully used to extract hydrological and tectonic
137 transient signals from GNSS displacements time series (Gualandi et al., 2017a; Gualandi et
138 al., 2017b; Serpelloni et al., 2018).

139 The output of this analysis is the definition of a limited number of sources, or components,
140 characterized by a specific spatial distribution (U) and following a specific temporal evolution
141 (V). A weight coefficient S (in mm) is necessary to rescale their contribution in explaining the
142 original data. Each independent component (IC) is described by a mix of Gaussians, which
143 allows for more flexibility in the description of the sources with respect to classical
144 independent component analysis (ICA) techniques. It allows to consistently take into account
145 missing data in the data set (Chan et al., 2003) and provides an estimate of the uncertainty
146 associated with each IC. The displacement time series at a given station can be
147 reconstructed by linearly summing up the contributions from all the ICs, each of which is
148 obtained by multiplying the specific spatial distribution by the associated weight times the
149 temporal evolution.

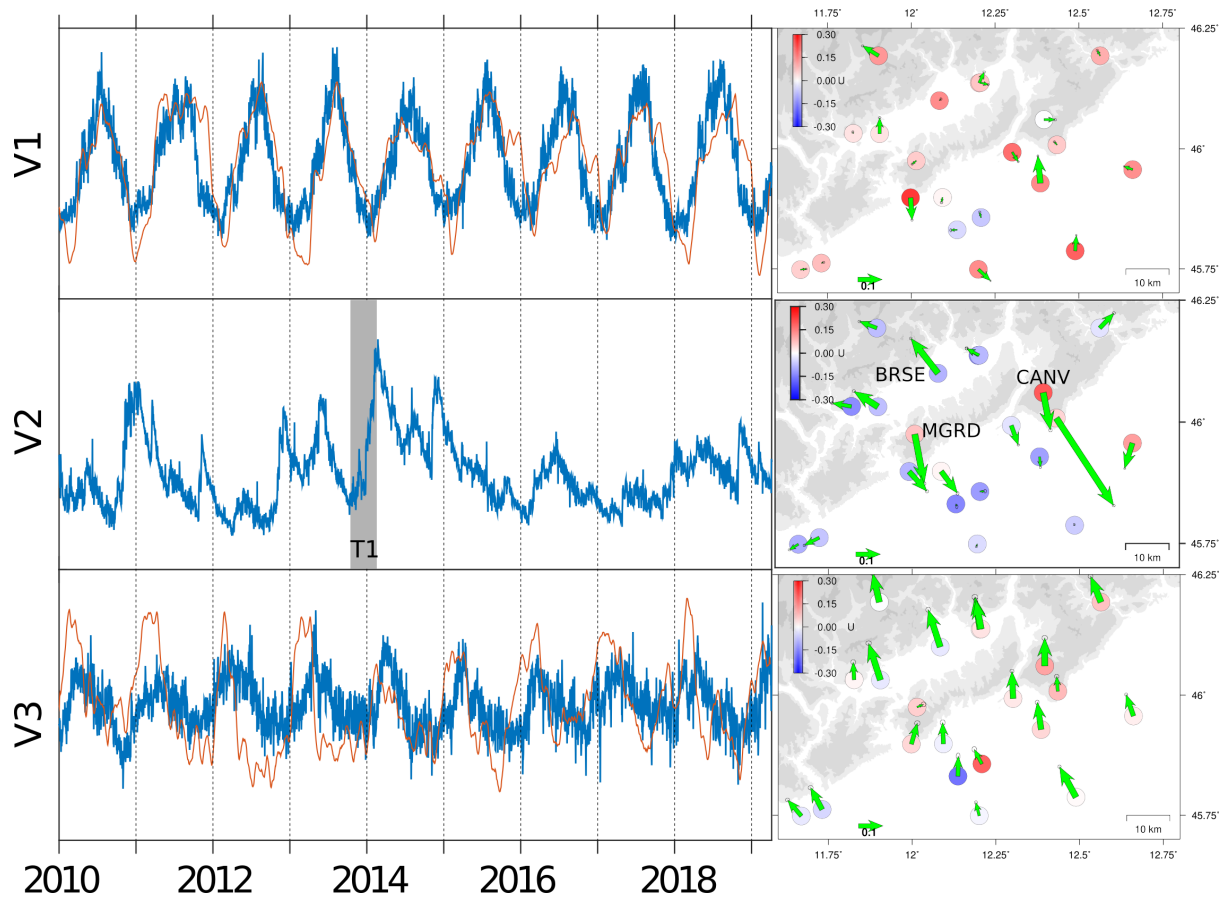
150 With the goal of reducing the correlation of the dataset, making the search of the IC direction
151 easier (Gualandi et al., 2016), the original time series are initially detrended. Differently from
152 previous works using this approach, the trend of each GPS station is estimated in a
153 multivariate statistical manner, by applying a vbICA analysis on displacement-time series
154 realized in a Adria-fixed reference frame, as described in the Supplementary material S1.2.
155 This approach is effective in removing the linear trend in case of strong non-linear signals
156 and short time-series.

157 Once detrended, according to the F-test, 3 ICs are necessary to satisfactorily reconstruct the
158 observed displacements. The temporal evolution (V) and spatial responses (U) of the three
159 ICs are shown in Fig. 2. Seasonal annual displacements in the vertical and NS directions
160 (IC1 and IC3) occur in response to surface hydrological mass loading (Serpelloni et al.,
161 2018). A non-seasonal, horizontal transient deformation signal (IC2, Fig. 2), characterized by
162 spatially variable amplitudes and directions, causes GNSS stations to reverse the sense of
163 movement with time, resulting in a sequence of dilatational and compressional deformation
164 oriented about normal to the mountain front.

165 Serpelloni et al. (2018) found that the temporal evolution of this signal correlates, somehow,
166 with the history of cumulated precipitations at monthly timescales. Nonetheless, the link
167 between surface deformation and changes in groundwater content remains difficult to find,
168 because of the lack of water wells in the mountainous area and because of the limited
169 spatial extent of the area affected by this transient deformation. Equivalent water content
170 estimated from GRACE can provide only coarse spatial (Famiglietti et al., 2011) and
171 temporal resolution for this area (Supplementary material S2.4).

172 In the next section we will use a lumped parameter hydrological mode to estimate daily
173 changes of continental water content to be compared with the temporal evolution of IC2.

174



175 2010 2012 2014 2016 2018

176 **Figure 2.** Temporal evolution (V; in blue) of the three ICs defined from the vbICA analysis
 177 and the corresponding spatial response in the horizontal (green arrows) and vertical
 178 (coloured circles) components, respectively. The gray area indicates the time interval (T1 =
 179 October 10th, 2013 - February 22nd, 2014) for which ground displacements have been
 180 computed and shown in Fig. 3. The red lines superimposed to V1 and V3 represent the
 181 mean vertical and N-S displacements caused by surface mass loading, respectively,
 182 estimated from the ERA-interim (European Centre for Medium-Range Weather Forecasts,
 183 ECMWF reanalysis) model and provided by <http://loading.u-strasbg.fr> (Gegout et al., 2010).

184

185

186

187

188

189

190

191 3. Surface deformation and link with hydrology

192 Water redistribution on the continents implies several processes that cover a wide range of
193 spatial and temporal scales. At scales larger than several hundreds of kilometers, GRACE
194 satellite observations or land surface models, such as the GLDAS modeling platform (Rodell
195 et al., 2004), can provide a fair estimate of total water storage (TWS) changes and are
196 typically used to compute surface displacements (Craig et al., 2017). At local scale, ground
197 observations such as soil moisture and groundwater head can describe storage and pore-
198 pressure changes, but their spatial representativity is limited. At regional/meso-scale, water
199 storage observations are rare. River discharge, for example, is representative over the
200 drained area (i.e. catchment), but only represents one flux contributing to storage changes.
201 In this work, we consider a modeling approach to define meso-scale water storage changes,
202 which is driven by meteorological river discharge observations.

203 Water storage changes in a downstream sub-catchment (see Fig. S2.1 in the Supplementary
204 material) can be estimated based on the mass balance equation:

$$205 \quad dS/dt = P + Q_{in} - E - Q_{out} - Q_{gw} \quad (1)$$

206 where P , E , Q_{in} , Q_{out} , Q_{gw} are respectively precipitation, actual evapotranspiration,
207 incoming river inflow, outgoing river discharge, and potential groundwater import/export in
208 a surrounding basin. Among the different water fluxes, P , Q_{in} and Q_{out} can be measured,
209 while actual evapotranspiration and Q_{gw} should be estimated with a model. It is worth noting
210 that at regional scales (<100 km), lateral water fluxes could be significant, especially in a
211 mountainous region, where the convergence of water from steep basins to valleys with
212 gentle slopes favour transient accumulation of large amount of water. Such lateral flow
213 processes are hardly modeled within large-scale hydrological models.

214 The tool we use to estimate the right side factors of eq. 1 is the lumped parameter
215 hydrological model GR5J (Pushpalatha et al., 2011), which finally allow us to quantify daily
216 TWS changes at the scale of single hydrological basins (Fig. 3). The GR5J rainfall-runoff
217 model is based on two storage compartments, which mimic the typical response of soils and
218 groundwater to antecedent precipitation. This model is forced with precipitation, temperature
219 and potential evapotranspiration and computes actual river discharge. It is typically

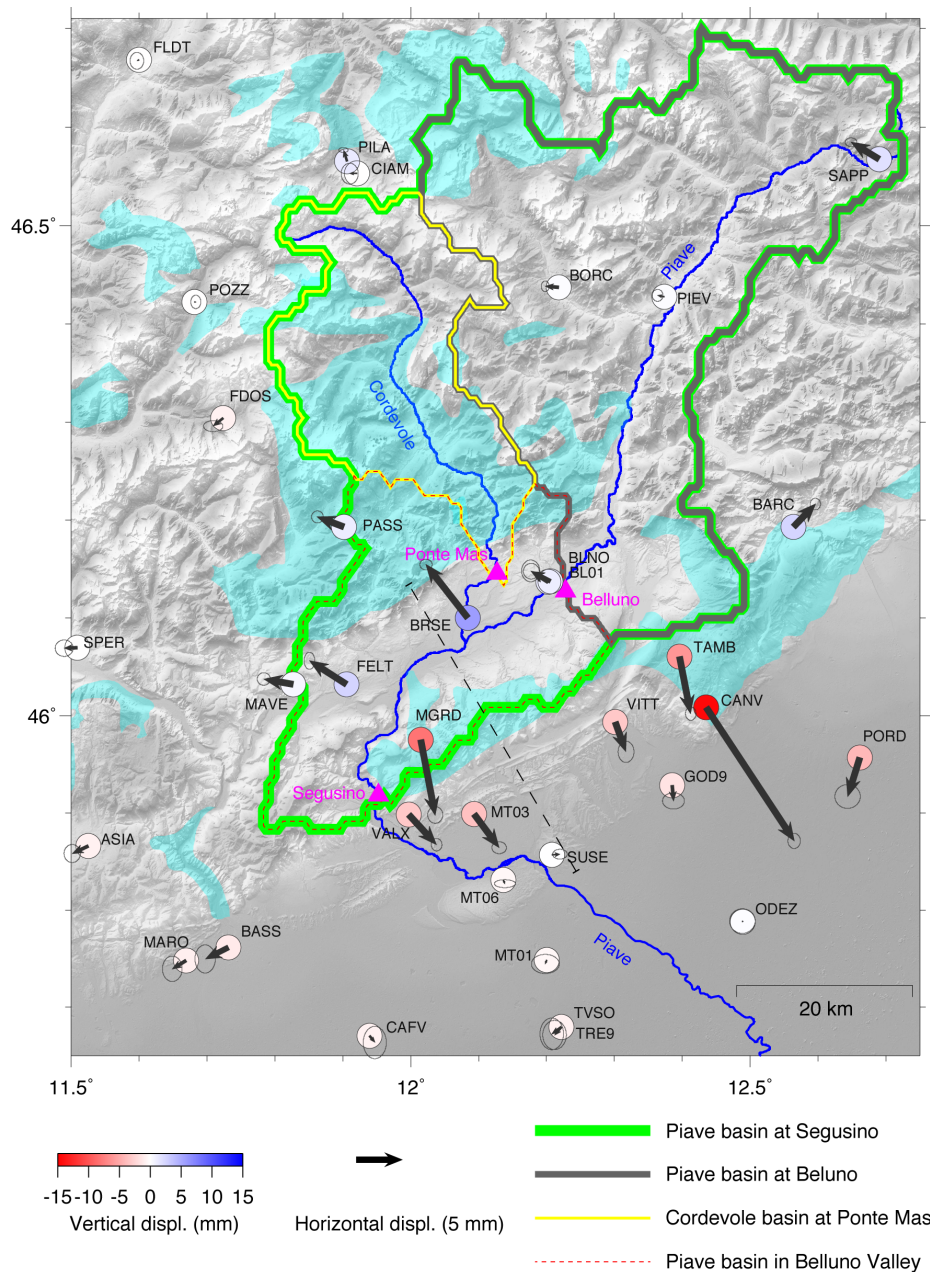
220 calibrated on observed river discharge to define the eight mathematical parameters defining
221 the dynamics of the two stores and their relations. The best set of parameters values is then
222 defined by a Marquard-Levenberg least squares regression analysis using root mean square
223 error on the logarithm of discharge as an objective function. As discharge vary over two
224 orders of magnitude, calibrating the model on the logarithm of the discharge is preferred to
225 ensure that both high and low flows have a similar weight. In the end, total water storage
226 changes is computed as the sum of both stores.
227 Since the GR5J inputs are a daily value of precipitation, temperature and potential
228 evapotranspiration, we estimate the precipitation and temperature value form January 1st,
229 2010 to March 31st, 2019 by computing a daily weighted mean of in-situ observations
230 managed by ARPAV (<http://www.arpa.veneto.it/bollettini/storico>), using the Thiessen polygon
231 method (Supplementary material S2.1). Potential evapotranspiration has been evaluated by
232 using the Jensen-Haise method (Jensen et al., 1990; Supplementary material S2.2).
233 In the study area we define three hydrological basins by using the drainage direction maps
234 available on www.hydrosheds.org/page/availability and watershed outlets located at the river
235 discharge measurements on the Piave river at Belluno, Segusino and of the Cordevole river
236 at Ponte Mas (see Fig. 3). The region of interest, though, is limited to a portion of a
237 watershed located in the Belluno Valley. Considering the availability of river discharge data
238 upstream and downstream this region, the model is calibrated and water storage changes
239 computed on each of the watershed (Supplementary material S2.3). The final TWS_{res} is set
240 as the storage difference between the largest basin (Piave at Segusino) and its subbasins
241 (Cordevole at Ponte Mas and the Piave at Belluno) as

$$242 \quad TWS_{res} = TWS_{seg} - (TWS_{cor} + TWS_{bel}) \quad (2)$$

243 Where TWS_{seg} , TWS_{cor} , TWS_{bel} indicate the TWS computed in the Piave at Segusino,
244 Cordevole at Ponte Mas and Piave at Belluno watersheds, respectively.

245 Fig. 4 shows that the normalized temporal evolution of the non-seasonal deformation signal
246 (V2) and TWS_{res} are clearly correlated (Pearson correlation coefficient = 0.83),
247 demonstrating that this transient deformation component is driven by changes in

248 groundwater contents. The agreement is good both during (rapid) TWS_{res} increase and
249 (slower) TWS_{res} decrease, either when small and/or slow TWS_{res} changes happen and during
250 extreme events. This process is also displayed in the Supplementary material V1.
251 On October 29th, 2018, storm Vaia, with >300 mm of cumulative precipitation in 72 hours
252 and wind gusts exceeding 200 km/h, hit north-eastern Italy, causing the loss of 8 million
253 cubic meters of standing trees. This extreme event is well recorded as a rapid increase of
254 TWS_{res} (dashed line in Fig. 4) corresponding to extensional deformation recorded by the
255 GNSS network, with the largest offsets at MGRD (~5 mm toward SE) and BRSE (~2.5 mm
256 toward NW).
257
258

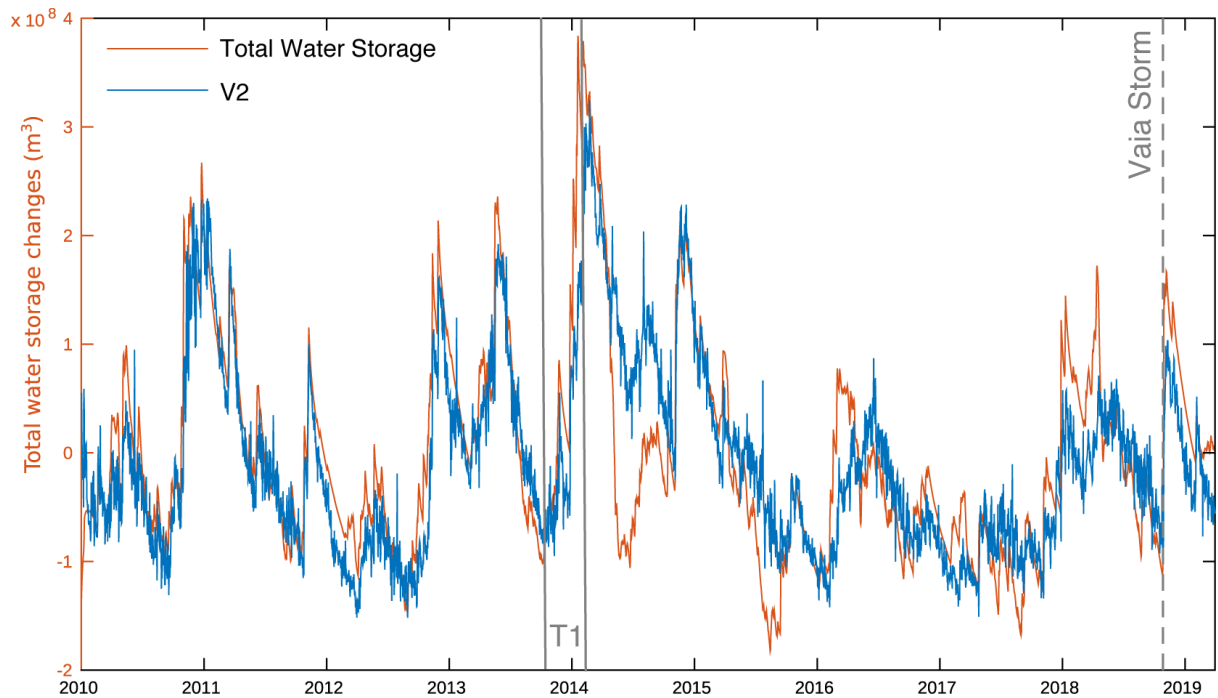


259

260 **Figure 3.** Hydrological map and geodetic displacements in the study region. Piave and
 261 Cordevole rivers (in blue) are gauged at three locations (purple triangles), defining three
 262 watersheds (yellow, green and grey) and the 883 km² region in-between (Belluno Valley, red
 263 dashed line) where water storage changes are modeled. Highly productive fissured karst
 264 aquifers are highlighted in cyan from the International Hydrogeological Map of Europe
 265 1:1,500,000 (<http://www.bgr.bund.de/ihme1500>). Regional horizontal (black arrows) and
 266 vertical displacements (color dots), described by the second source of independent
 267 component analysis (IC2) on 67 GNSS stations during T1 period (winter 2013-2014) are
 268 superimposed (see also Fig. 2). The dashed black line show the trace of the geological cross
 269 section of Fig. 5.

270

271



272

273 **Figure 4.** Temporal evolution of the modeled water storage changes in the Belluno Valley

274 (orange, left axis) and the geodetic IC2 (blue). The vertical black lines indicate the T1 period

275 and the epoch of the intense Vaia storm (dashed).

277

278

279 **4. Surface deformation and link with geology**

280 Transient displacements in the Alps have been interpreted as due to pressure changes

281 associated with water level variations in vertical karst fractures (Devoti et al., 2015;

282 Serpelloni et al., 2018). In this work we develop a two-dimensional finite-element model

283 (FEM) with the goal of testing different sources of deformation potentially able to

284 “accommodate” groundwater level changes in the Belluno Valley, comparing model results

285 with the ground displacement pattern associated with the hydrological deformation

286 component (Fig. 2). We use the “Solid Mechanics” physics module of the COMSOL software

287 (Supplementary material S3.1), considering the problem as quasi-static at daily time scales

288 and resolving the model as “stationary”. We built the 2D model on the basis of the

289 geological cross-section proposed by Galadini et al. (2005)
290 (the trace of the cross section is shown in Fig. 3), which is constrained by geological and
291 geophysical information, and is in agreement with local seismicity (Danesi et al., 2015;
292 Romano et al., 2019) and seismic prospections (Fantoni et al., 2002). The cross section is
293 normal to the strike of the MCCV mountain range, that is about parallel to the directions of
294 geodetic displacements associated with IC2 (Fig. 2). We considered the GNSS stations
295 located within 20 km from that cross section (considering a length of ~40 km of the Belluno
296 Valley), whose positions and displacements are projected along the direction of the profile
297 (Fig. 5). We focus on a specific time interval (October 10th, 2013 - February 22nd, 2014; T1
298 in Fig. 2 and Fig. 4), corresponding with a period of rapid increase of TWS_{res} and extensional
299 deformation (Fig. 2).

300 The FEM model allows us to account for topography and subsurface geological features of
301 the area, in particular the presence of faults and the different mechanical properties of the
302 rock layers. The rock mechanical parameters used (Supplementary Table S3.1), in particular
303 the Young modulus and Poisson's ratio, are taken from Anselmi et al. (2011).

304 The different models we tested to describe the relation between TWS_{res} changes and the
305 deformation associated with IC2 (Fig. 6) are based on the assumption that the pressure
306 variations caused by the accumulation of water are directly proportional to the TWS_{res}
307 changes. We consider two main families of water pressure distribution:

308 1) models where pressure is distributed horizontally and applied vertically on the elastic
309 domain: the loading caused by water storage changes in an unconfined aquifer, hosted by
310 the Belluno Basin Units, cause a downward pressure on the aquiclude (impermeable layer,
311 here the Igne Formation) at the base of the aquifer (Model 1). We also take into account the
312 possible role of the Bassano-Valdobbiadene backthrust (BVBT) and BVT faults as lateral
313 aquiclude (Model 2). In Model 3 we represent the surface loading on the Belluno Valley,
314 assuming storage changes in a very shallow water reservoir, localized along the Piave river
315 bed.

316 2) models where pressure is distributed vertically along sub-vertical structures and applied
317 orthogonally in the modeled domain: Model 4, 5 mimic the impact of pressure changes in a

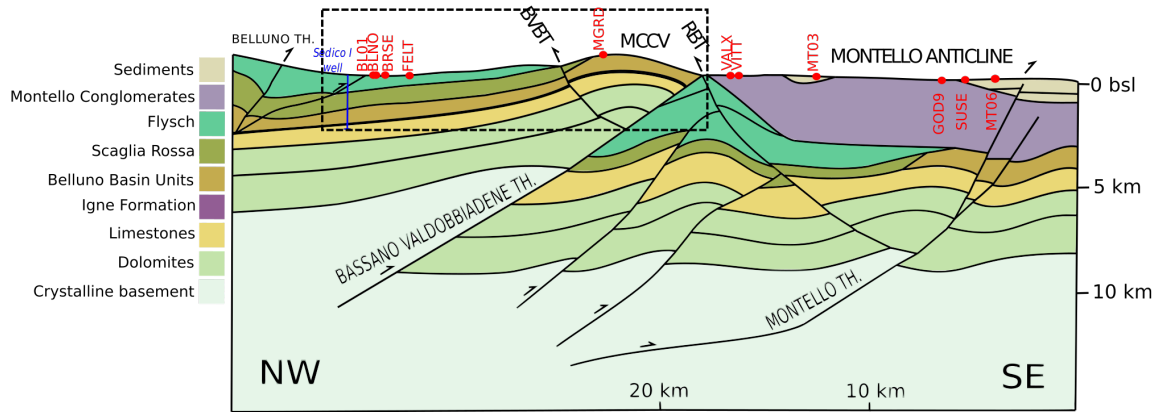
318 single open fracture reaching the surface, which represents the network of fractured rocks in
319 the damage-zone associated with the BVT and the BVBT faults, respectively. Fault damage
320 zones in the carbonate rocks, in fact, are often host to open fractures (karst), demonstrating
321 that they can also be conductive to fluid flow (Torabi et al., 2019). Transient pressure
322 changes are applied on the whole fracture, following Longuevergne et al. (2009). Such
323 behavior has been validated in fractured karstic systems in Lesparre et al. (2017).

324 We use two criteria to evaluate how well a model reproduce the displacements pattern
325 associated with IC2 (Figure S3.3). The first is the ratio between vertical and horizontal
326 displacement at each GNSS station, which should not significantly exceed 1; the second is
327 the number of stations with the horizontal displacements pattern in agreement in sign with
328 IC2. According to these criteria, the displacements pattern associated with IC2 is better
329 reproduced by the models where pressure is distributed vertically than the ones where
330 pressure is distributed horizontally. In fact the vertical displacements generated by the
331 Models 1, 2 and 3 are too large compared to the horizontal ones, and the horizontal
332 displacements pattern shows significant disagreement with the one associated with IC2 (Fig.
333 2). A detailed analysis of each tested model, in terms of fit of the horizontal and vertical
334 displacements, can be found in the Supplementary material S3.2.

335 The model that best reproduces the horizontal and vertical displacements is Model 5 in Fig,
336 6. Here the fracture is considered hydrologically conductive (Faulkner et al., 2010) down to 0
337 m a.s.l where it intersects an impermeable formation (the Igne Formation), as we will discuss
338 in section 6.1.

339

340



341

342 **Figure 5.** Geological cross section of the study area, modified from (Galadini et al., 2005);

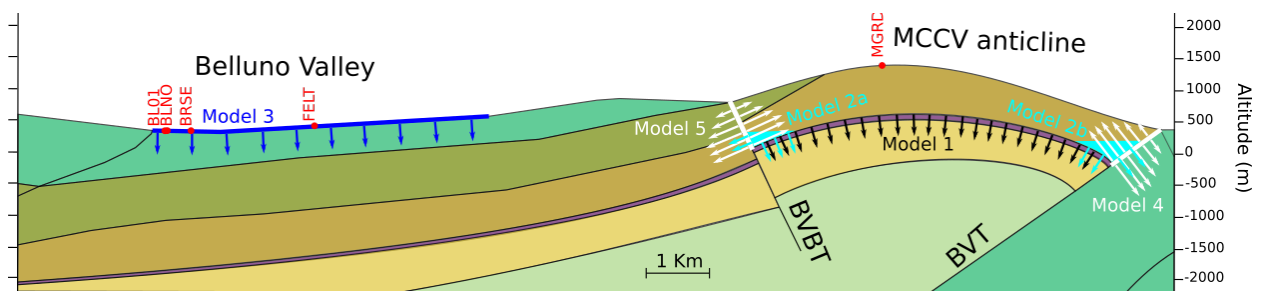
343 red dots: position of the GPS stations projected along this profile. RBT: Revine backthrust;

344 BVBT: Bassano-Valdobbiadene back thrust. The dashed rectangle represents the area

345 shown in Fig. 6.

346

347



348

349 **Figure 6.** Zoom on the 2D model cross-section of Fig. 5, showing a schematic

350 representation of the tested models used to explain the horizontal displacements

351 reconstructed by IC2. MCCV: Mount Cesen-Col Visentin anticline; BVT: Bassano-

352 Valdobbiadene thrust; BVBT: Bassano-Valdobbiadene backthrust. Rock formations are

353 shown with the same legend of Fig. 5.

354

355

356

357

358

359

360 **5. Hydrological control of seismicity**

361 In Section 3 we demonstrate the link between hydrology and surface deformation (Fig. 3)
362 and in Section 4 we provide a physical model explaining this process. In this section we
363 investigate and test possible relationships between changes in TWS_{res} and seismicity rates.
364 We use the local earthquake catalogue from Romano et al. (2019), which contains high-
365 resolution relocations of events with magnitudes ranging from -0.8 to 4.5, in the period
366 January 2012 to October 2017. This catalog was produced using data from the Collalto
367 Seismic Network (Priolo et al., 2015).

368 Before exploring any possible link between seismicity rates and hydrological data, we
369 identify and remove the aftershock events that are more likely associated with earthquake
370 stress triggering processes. This analysis is performed by declustering the catalog in the
371 time domain using the epidemic-type aftershock sequences model ETAS (Ogata, 1998). The
372 resulting partition between background seismicity and aftershocks is presented in Fig. 7a.
373 More details of this process are presented in the Supplementary material S4.1.

374 It is worth noting that in the ETAS model the background seismicity is assumed to be
375 generated by a homogeneous Poisson process and is physically associated with a constant-
376 rate tectonic loading process. However, the ETAS-based declustering process does not
377 guarantee that the resulting background seismicity is actually stationary (Console et al.,
378 2010), as a result it is actually possible to observe temporal fluctuations in the background
379 seismicity obtained after the temporal declustering process. This departure from stationarity
380 is supposed to be caused by the temporal activation or quiescence of seismic sources
381 forced as a result of processes having a physical cause outside the stationary tectonic
382 loading assumed by ETAS (Zhuang et al., 2002).

383 In this paper we explore possible correlations between temporal variations in hydrological
384 data and the background seismicity. With this aim, we adopt the covariate model proposed
385 by Garcia-Aristizabal (2018), which allows us to perform a robust statistical evaluation of
386 possible relationships between TWS_{res} changes (x_{TWS}) and background seismicity rates.
387 According to this model, when the forcing process generating the seismicity in a given zone
388 is stationary in time (as e.g., a constant tectonic loading), the background seismicity rates

389 can be stochastically modelled using a homogeneous Poisson process; it implies that
 390 seismicity rates follow the Poisson distribution and, consequently, the times between
 391 consecutive events (inter-event times, t_{IET}) follow the exponential distribution. However, if
 392 the forcing process is non-stationary, and if it is possible to identify measurable parameters
 393 as *proxies* of the processes driving such non stationary behavior, then it is possible to model
 394 correlations between changes in seismicity rates and changes in the proxy parameters by
 395 linking them as covariates of the stochastic model parameters. In order to explore this
 396 possibility we set the exponential distribution as the basic template function for modelling the
 397 distribution of t_{IET} :

$$398 \quad f(t_{IET}|\mu(x_{TWS})) = \frac{1}{\mu(x_{TWS})} \exp\left(\frac{-t_{IET}}{\mu(x_{TWS})}\right) \quad (3)$$

400 and the possible dependencies on hydrological data (in this case x_{TWS}) are modelled writing
 401 the μ parameter of the exponential distribution in terms of deterministic functions of x_{TWS} of
 402 the explanatory covariate (Supplementary material S4.3). x_{TWS} is measured respect to a
 403 reference TWS_{res} assumed to be the minimum value reached by this parameter in the
 404 analysed period. In practice, we test polynomial functions relating $\log(\mu)$ and x_{TWS} as
 405 follows:

$$406 \quad \log[\mu(x_{TWS})] = \sum_{j=0}^n \alpha_j (x_{TWS})^j \quad (4)$$

408 where $\alpha_j = (\alpha_1, \alpha_2, \dots, \alpha_n)$ is a vector of coefficients of the polynomial function relating the μ
 409 parameter of the exponential distribution with the selected covariate x_{TWS} . We study in
 410 particular two competing models: the case $n=0$ represents a stationary model (i.e., non
 411 dependence on x_{TWS}), whereas the case $n=1$ represents a log-linear relationship (that is, an
 412 exponential relationship between μ and x_{TWS}). The input data are pairs of t_{IET} and the
 413 respective x_{TWS} averaged in a Δt time window (for which we test different values ranging

414 from days to weeks). The inference of model parameter values is performed using a Markov
415 chain Monte Carlo method, and the selection of the preferred model is performed calculating
416 the Bayes factor (Garcia-Aristizabal, 2018). A more detailed description of this model is
417 presented in the Supplementary material S4.3.

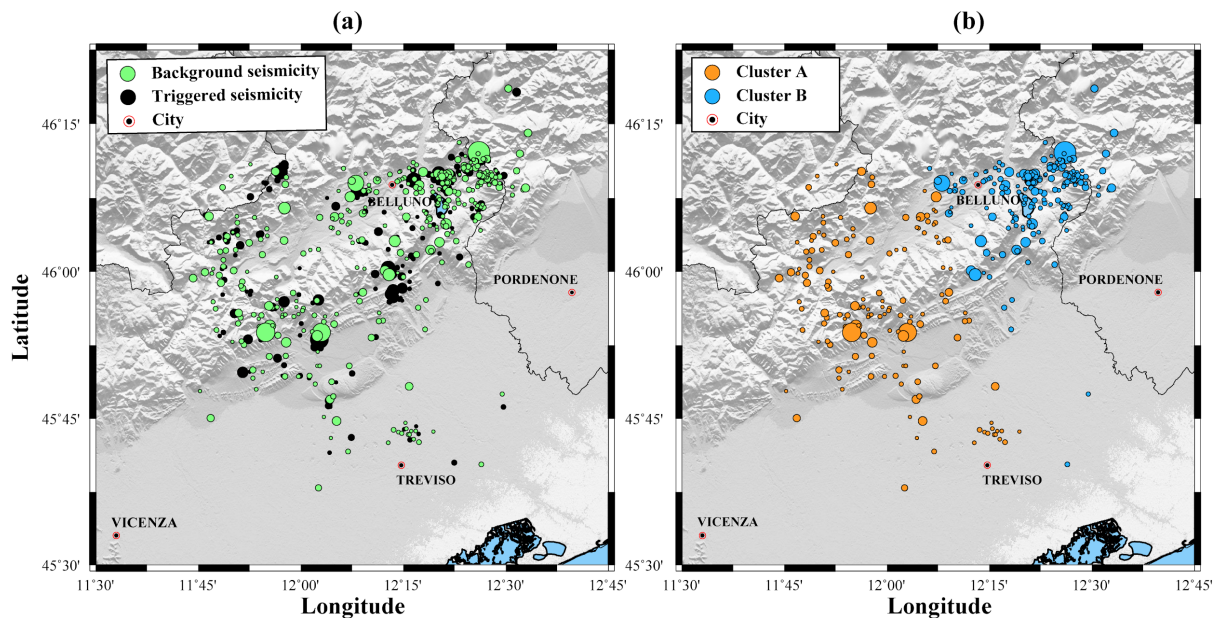
418 When considering the whole catalog of background seismicity (Supplementary Figure S4.2),
419 the Bayes factor indicates that there is not significant evidence to support a non stationary
420 model (Supplementary Table S4.2 and S4.3). However, the area covered by the earthquake
421 catalogue is characterized by different active faults systems and we hypothesize that these
422 fault systems could exhibit different responses to eventual stress perturbations related to
423 hydrology. A visual inspection of the earthquake locations (Fig. 7a) allows us to note a high
424 concentration of event locations in the NE part of the domain, whereas the seismicity
425 towards the SW part of the domain tends to be more evenly distributed.

426 To quantitatively identify possible spatial sets of seismicity we implement a cluster analysis in
427 the spatial domain (Supplementary material S4.2) using the k-means algorithm (MacQueen,
428 1967); the optimum cluster partition is selected using the Silhouette approach (Rousseeuw,
429 1987). We find that the background seismicity can be partitioned into two main clusters (Fig.
430 7b): (i) cluster A (orange points), located in the SW part of the domain, where earthquakes
431 can be associated with the Montello thrust and the BVT faults (Danesi et al., 2015); (ii)
432 cluster B (blue points), located in the NE part of the domain, in which most of the seismicity
433 can be associated with the N-dipping Cansiglio thrust fault (Galadini et al., 2005; Fig. 1b).
434 This preferential cluster partitioning roughly reflects the two main features that we observed
435 in the spatial distribution of the seismicity: a set of events mostly grouped in the NE part, and
436 a more evenly distributed seismicity towards the SW.

437 The correlation analysis using the covariate approach is then performed using the data from
438 each spatial cluster of background seismicity. Comparing plots of the moving average of
439 both TWS_{res} and the rate of seismic events (calculated in 90-days length time windows
440 sliding at increments of 1 day) for cluster A (Fig. 8a) and cluster B (Fig. 8b), we observe that
441 only the seismicity rate in cluster A tends to change in agreement with the changes in the
442 TWS_{res} . This observation is quantitatively confirmed by the covariate analysis

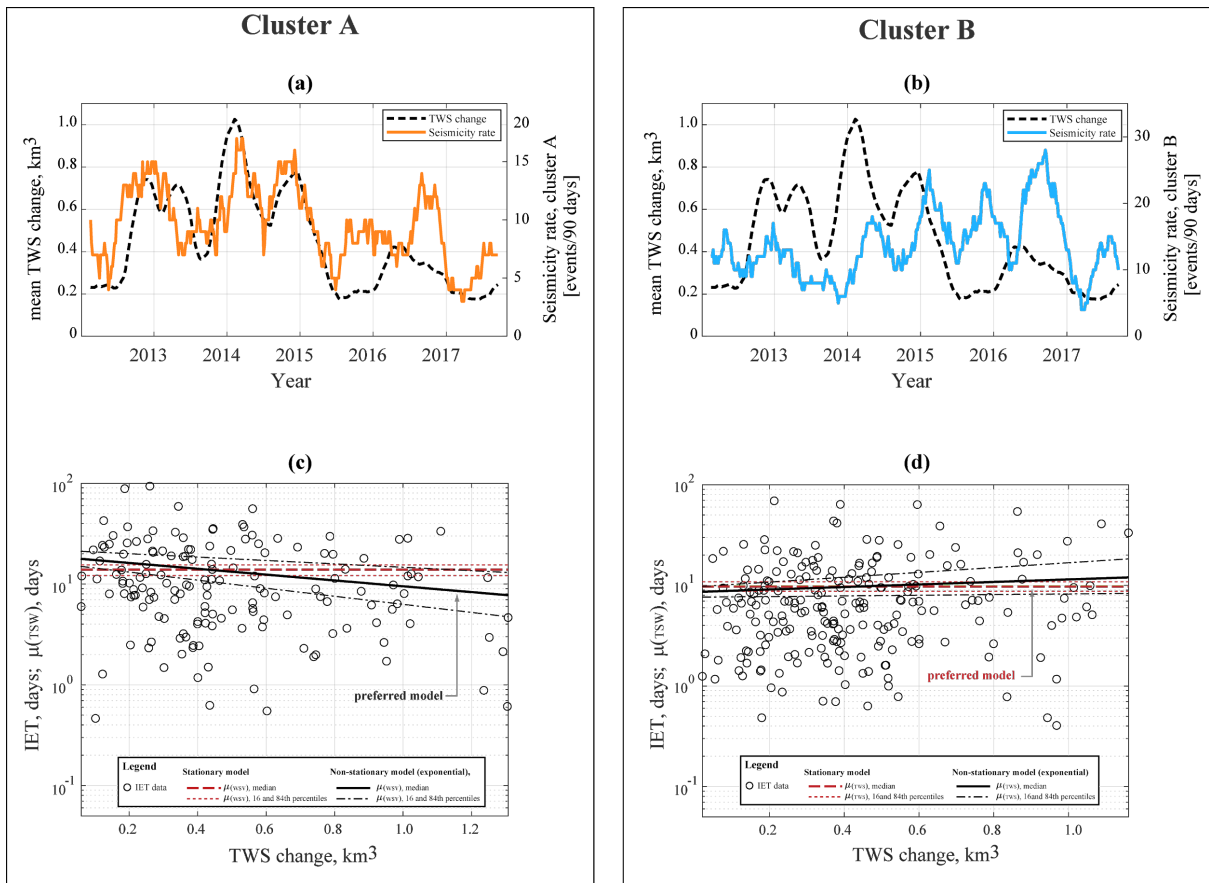
443 (Supplementary material S4.3), with the Bayes factor indicating that only for cluster A the
444 non stationary model performs better than the alternative stationary solution (Supplementary
445 Table S4.3). In fact, for the cluster A (i.e., the seismicity associated with the Montello thrust
446 and the BVT faults) there is positive evidence supporting a log-linear relationship between
447 the seismicity rate (modelled through the distribution of inter-event times, t_{IET}) and the TWS_{res}
448 changes, in contrast to a stationary reference model (Fig. 8c). On the other hand, for cluster
449 B the evidence supports the stationary model (Fig. 8d), indicating a not significant link
450 between seismicity rates in the Cansiglio thrust fault zone and TWS_{res} changes in the Belluno
451 Valley. The parameter values of the fitted models are summarized in the Supplementary
452 Table S4.4.

453



454
455 **Figure 7. (a)** Seismicity in the study area, separated as background (green circles) and
456 triggered (black circles) seismicity according to the ETAS model. **(b)** Clusters (A and B) of
457 background seismicity identified using spatial cluster analysis.

458



459

460 **Figure 8.** Moving average TWS (discontinuous black) and rate of seismic events in (a)
 461 cluster A (continuous orange) and (b) cluster B (continuous blue), calculated in 90-days
 462 length time windows sliding at increments of 1 day. Plot of inter-event times in (c) cluster A
 463 and (d) cluster B against TWS changes, and the results for the two tested models: stationary
 464 model (red) and Log-linear (black). Preferred models are indicated with the arrow in (c) (d).

465

466

467

468 6. Discussion

469 6.1 Hydromechanical coupling

470 In Sections 3 and 4 we described the link between hydrological processes and solid Earth
 471 deformation by the joint interpretation of hydrological and mechanical models results,
 472 constrained by geodetic, hydrological, meteorological observations and
 473 geological/geophysical information on subsurface structural and tectonic settings. We
 474 propose a possible mechanism able to explain water accumulation in a narrow, subvertical,
 475 geological structure and reproduce the horizontal anisotropic extensional deformation

476 observed during a phase of large water storage increase. The same mechanism is assumed
477 to be able to explain smaller deformation associated with phases of smaller TWS_{res} increase,
478 and, with inverted sign, to explain the observed compressional deformation during phases of
479 TWS_{res} decrease, responding to the fast dynamics of karst systems.

480 In our interpretation, we make the assumption that water level variations in rock fractures, or
481 faults, are directly linked to the amount of water stored in the subsurface, which includes
482 also water stored in the soil (i.e, soil moisture). However, the correlation between V2 and soil
483 moisture values, as calculated from GLDAS Noah in the Piave at Segusino basin, is much
484 lower (Pearson correlation coefficient = 0.18; see Figure S2.4 in the Supporting material)
485 than the correlation between V2 and TWS_{res} (Pearson correlation coefficient = 0.83),
486 suggesting that the greatest contribution to the measured transient geodetic displacements
487 comes from groundwater, stored in karst rocks.

488 We assume that the network of damage-zone faults, which we model as a single fracture
489 associated with BVBT in Model 5, are well connected and water-saturated; the water level
490 varies as the TWS_{res} , causing pressure changes orthogonal to fracture walls. It is likely that
491 the water feeding the fracture mainly comes from the top of the MCCV mountain chain: the
492 higher fracture density at the hinge zone of the anticline (Feng and Gu, 2017) and the well-
493 developed epikarst in the exposed rock formations (Maiolica and Rosso Ammonitico)
494 suggest the presence of an epikarst circulation on the top of MCCV chain (Klimchouk and
495 Sauro, 1996). The combined effect of the epikarst and the presence of a shallow, low
496 permeable layer (the Fonzaso formation, located at ~200 m of depth from the surface)
497 facilitates the rapid infiltration of precipitation water and its flow toward the backthrust,
498 following the northward inclination of rock layers and stratification; this hypothesis is
499 supported by the observed lack of a time-delay, at the daily time scale, between TWS_{res} and
500 the geodetic deformation signal (Fig. 4). However, we can not exclude that water can flow
501 southward, toward the BVT, which might behave similarly to the backthrust as an
502 hydrologically active structure (Supplementary material S3.2, Model 4). Nonetheless, the site
503 MGRD (Fig. 1a) moves toward the BVT and away from the backthrust when TWS_{res}
504 increases, implying that an hydrologically active BVT is likely to have a secondary effect with

505 respect to its backthrust.

506 A more precise description of the source of deformation, which includes the identification of
507 both the fracture bottom position and the water level rise inside it, is not straightforward
508 because of the trade-off between fracture width and its opening (e.g., Silverii et al., 2016;
509 Devoti et al., 2015). Nonetheless, because of the lack of evidences of aquifers reaching
510 depths that are hundreds of meters below the sea level surface, and since the maximum
511 water level variation measured in a similar karst system is ~300 m (Milanovic, 2005), we
512 assume the bottom position of the fracture at 0 m above sea level, at the interface between
513 the Vajont limestone and the more impermeable Igne formation (see Fig. 6). Once set the
514 bottom position of the fracture, the water level rise that provides the best match between
515 modeled and observed displacements is 100 m (Fig. S3.3), with the water level inside the
516 fracture located at about 10 m below the free surface when V2 reaches its maximum during
517 the analyzed time-period (i.e., January, 2014). Furthermore, we analyze the effect of the
518 initial opening of the fracture when applying the same pressure values on its walls; we have
519 found that assuming different initial opening values does not impact significantly the resulting
520 displacements (Fig. S3.4). It follows that it is not possible to quantify the volumes of water
521 involved, since the only quantity affecting the displacements is the water level variation,
522 while the initial fracture opening does not play a key role.

523 Although the 2D numerical model used is an acceptable simplification, given the spatial
524 distribution and density of available geodetic data, we are aware of its limitations. We are
525 assuming that geological features (including for example outcropping formations, fracture
526 spacing, strike of faults and fractures, topography) are constant along the SW-NE direction,
527 for about 40 km, which is not necessarily true. A 2D model cannot take into account the fact
528 the the MCCV mountain chain and associated thrust and back thrust faults curve north,
529 going into the Fadalto valley (see Fig. 1). More importantly, changes in water level along the
530 backthrust are implicitly assumed to be uniform along its strike in a 2D model, but an
531 heterogeneous change in water level can cause more localized deformation signals, which
532 would be however difficult to detect with the present GNSS network configuration. Moreover,
533 effects associated with similar processes occurring at nearby karst systems cannot be taken

534 into consideration. Hydrological deformation in the Cansiglio plateau, in fact (Devoti et al.,
535 2015; Serpelloni et al., 2018) may affect GNSS sites VITT and GOD9 (Fig. 1). Additional
536 GNSS stations will be necessary to overcome these problems.

537

538 **6.2 Seismotectonic implications**

539 Two main mechanisms have been suggested to explain hydrological modulation of
540 seismicity: variations in pore-fluid pressure at hypocentral depths (Hainzl et al., 2006) and
541 direct stress on the fault plane (Bettinelli et al., 2008; Craig et al., 2017; Johnson et al., 2017;
542 D'Agostino et al., 2018). In the latter case, there is usually a little or no time delay between
543 hydrological indicators and seismicity rate. In the former, seismicity rate variations are
544 usually delayed with respect to hydrological observations by a time lag, which is strictly
545 dependent on the earthquake nucleation depth and on the hydraulic diffusivity of the material
546 between the surface and the seismicity source. The lack of temporal delay between the
547 seismicity rate and the TWS_{res} (Fig. 4) excludes an important role for poroelastic
548 contributions, making direct effect of stress changes at seismogenic depths the most likely
549 process linking hydrology and seismicity.

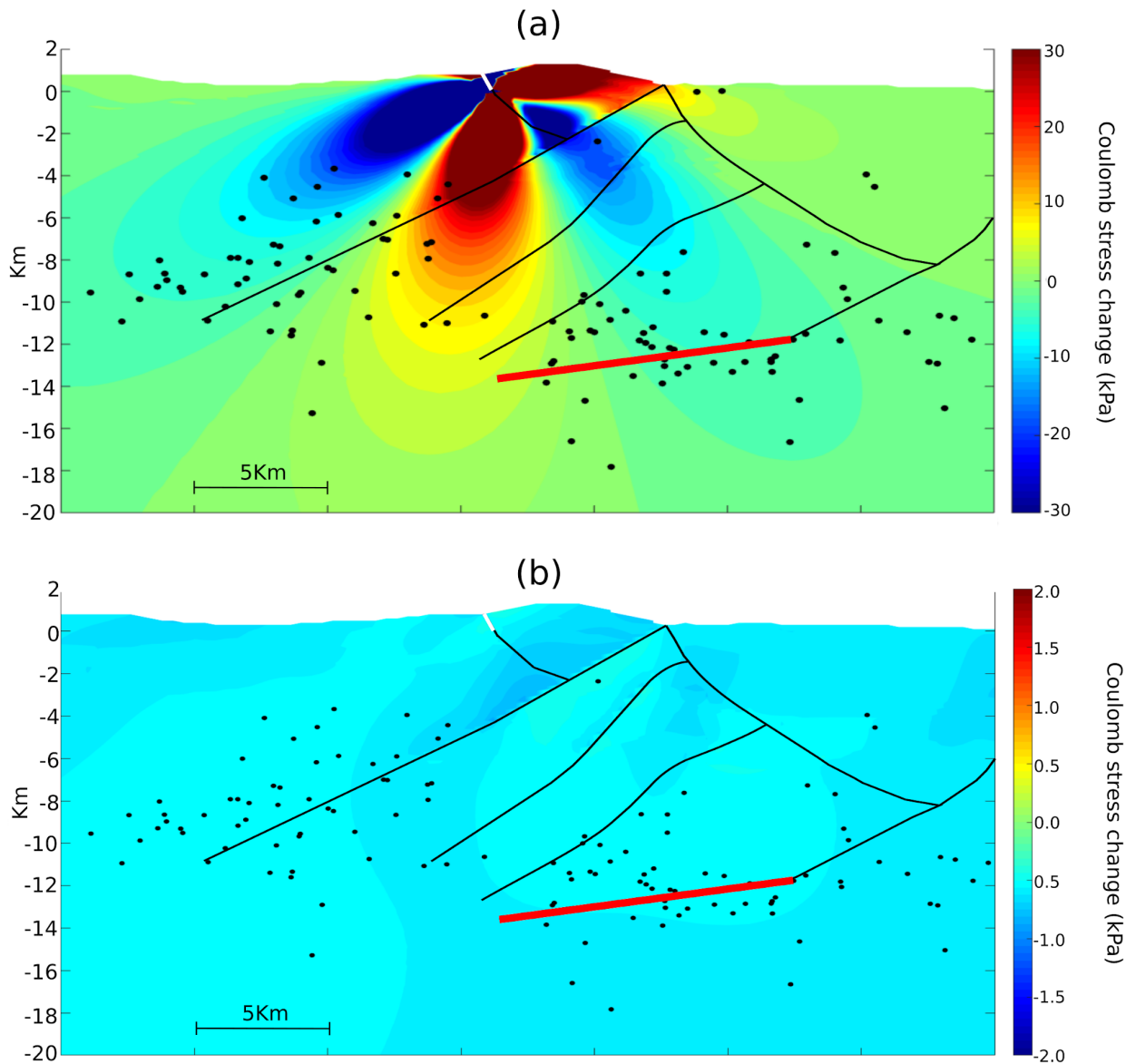
550 In case of seasonal stress perturbations, seismicity rates can correlate either with the stress
551 values or with stress rates, depending if the period of the stress perturbation (T_p) is smaller
552 or larger than a critical period (T_d), which in turn is controlled by the loading plate velocity
553 (Ader et al., 2014). The period that dominates the temporal evolution of stress in the study
554 area is 1 yr (Supplementary Figure S2.5), which is a value that T_d reaches only in rapidly
555 deforming regions (Bettinelli et al., 2008). In slowly deforming regions, as the Southern Alps,
556 T_d usually assumes larger values. This observation is consistent with our findings, implying
557 that stress changes are proportional to the magnitude of the TWS_{res} and not to its time
558 derivative (which represents whether TWS_{res} is in an increasing or decreasing phase).

559 We estimate the stress change associated with the deformation caused by the water
560 pressure increase (T1 time window in Fig. 4) in the hypothesized fracture source. In practice,
561 we calculate the Coulomb failure function (CFF, Supplementary material S3.3) on receiving

562 planes oriented in agreement with the compressional tectonic regime of the area. Fig. 9a
563 shows CFF values assuming a shallow-dipping (10°) decollement (i.e. the Montello flat) as
564 receiving source, showing that in the depth interval where most of the seismicity associated
565 with cluster A (see Fig. 7b) is located (4-14 km), positive stress changes are up to 25 KPa.
566 These stress changes are larger than stressing rates from tectonic loading, which are
567 expected to be of the order of 1-3 KPa (Caporali et al., 2018). Similar values are obtained,
568 but with different spatial patterns, assuming different thrust-receiving sources; however, a
569 correlation between areas of stress increase and seismicity is not evident. Unfortunately, the
570 faulting mechanisms of the background seismicity are not well constrained, and the focal
571 mechanisms available for other events in the catalogue (Romano et al., 2019) show a large
572 range of mechanisms, including normal, thrust and strike-slip faulting on different planes. So,
573 while a clear spatial correlation between seismicity and regions of positive stress increase is
574 not apparent, it is likely that the highly deformed upper crust, inherited by the complex
575 tectonic evolution of the Southern Alps (Castellarin and Cantelli, 2000), provides
576 heterogeneous response to the hydrologically-modulated stress changes.

577 It is however important to note that the amplitude of the CFF field generated by the TWS_{res}
578 increase in hydrologically active fracture is much larger than the one generated by the
579 annual surface hydrological mass loading (Fig. 9b), which actually is considered as the main
580 mechanisms that modulate seismicity rates in other regions (Hainzl et al., 2014; Johnson et
581 al., 2017), where, however, much greater annual vertical displacements, and consequently
582 greater seasonal stress perturbations than those observed in the Alps, are present.

583



584

585 **Figure 9. (a)** Coulomb stress change during a phase of TWS_{res} increase (T1 in Fig. 4)
 586 caused by a source of deformation as in Model 5 (see Supplementary material S3.2),
 587 considering planes parallel to the Montello decollement (dip angle= 10°), highlighted in red.
 588 **(b)** Coulomb stress change calculated on the same dipping planes considering as source of
 589 deformation a 1 kPa uniform load on the free surface. This value causes a subsidence of
 590 ~ 3.8 mm, which is consistent with the amplitude of the vertical displacements caused by the
 591 large scale superficial loading in the time interval that goes from summer to winter (see Fig.
 592 2) and inhibits thrust faulting (negative CFF values in all the domain). The black dots
 593 represent the background seismicity of cluster A.

594

595

596 **7. Conclusions**

597 Using geodetic, hydrological and meteorological data, integrated into hydrological and
598 mechanical models, we show how water converging from a large drainage area (~1000 km²)
599 toward a specific zone, can generate horizontal surface displacements that are
600 superimposed to surface hydrological and tectonic loading. Our results demonstrate that
601 hydrologically-active and seismically-active faults can be totally disconnected, and that
602 stress transfer is a critical mechanism for triggering seismicity at depths reaching more than
603 10 km below the surface. We show that hydraulic pressure changes in a shallow fracture (<1
604 km) can generate large shears (~10 kPa) in faults oriented orthogonally and at distances of
605 the order of ~10 km (horizontally and vertically). In such a context, the link between
606 hydrology and seismicity is favoured by 1) the existence of a (shallow) hydrologically-active
607 fracture connected to the surface; 2) the existence of properly oriented (orthogonal),
608 seismically active structures (such as a classical thrust/backthrust couple), and 3) water
609 convergence from a watershed/river basin towards the hydrologically active structure,
610 leading to large water storage (and therefore water pressure) changes. In such contexts,
611 horizontal deformation is best suited to highlight physical links between surface deformation
612 and hydro-mechanical processes occurring at depth.

613

614

615

616 **Acknowledgements**

617 We thank L. Anderlini for helpful discussions and suggestions on stress analysis and E.
618 Scoccimarro for suggestion on the analysis of pluviometric data.

619

620 **Author contributions**

621 F.P. conceived and led the paper and performed numerical and hydrological modeling. E.S.
622 coordinated the study and analyzed GNSS data. L.L. supervised hydrological modeling and
623 interpretation. A.G.A and L.F. performed the analysis of the earthquake catalogue. M.E.B.

624 cross-examined the results and supervised F.P. PhD. A.G. supervised the analysis of GNSS
625 displacements. L.D. supported hydro-geological interpretation. F.P., E.S., L.L., A.G.A. and
626 L.F wrote the paper. All the authors discussed the content of the paper and shared the
627 writing.

628

629 **Competing interests**

630 The authors declare no competing interests.

631

632 **Data availability**

633 Precipitation, temperature and river flow data are provided by “Agenzia Regionale per la
634 Prevenzione e Protezione Ambientale del Veneto” (ARPAV):
635 https://www.arpa.veneto.it/bollettini/storico/Mappa_2019_TEMP.htm.

636 Extraterrestrial irradiance data are available from [http://www.soda-pro.com/web-](http://www.soda-pro.com/web-services/radiation/extraterrestrial-irradiance-and-toa)
637 [services/radiation/extraterrestrial-irradiance-and-toa](http://www.soda-pro.com/web-services/radiation/extraterrestrial-irradiance-and-toa).

638 Drainage direction maps used to define river basins are available on
639 www.hydrosheds.org/page/availability.

640 The analyzed seismic catalog is available in the supplementary material of Romano et al.
641 (2019).

642 We use publicly available raw GNSS data. However, RINEX data can be requested to E.S.,
643 if not yet available on the original repositories.

644 Raw GPS time series are available on <https://doi.org/10.1594/PANGAEA.912895>

645 The Collalto Seismic Network data are available on <https://doi.org/10.7914/SN/EV>.

646 **Code availability**

647 The MATLAB code for TWS estimation and vbICA decomposition are available from the
648 corresponding author on request.

649

650 Founding source

651 This work was supported by the project TRANSIENTI, founded by the Italian Ministry of
652 Education, Universities and Research (MIUR) “Premiale 2014”.

653

654

655 References

656 Ader, T.J., Lapusta, N., Avouac, J.-P., Ampuero, J.-P., 2014. Response of rate-and-state
657 seismogenic faults to harmonic shear-stress perturbations. *Geophys. J. Int.* 198, 385–
658 413. doi:10.1093/gji/ggu144

659 Anderlini, L., Serpelloni, E., Tolomei, C., De Martini, P.M., Pezzo, G., Gualandi, A., Spada,
660 G., 2020. New insights into active tectonics and seismogenic potential of the Italian
661 Southern Alps from vertical geodetic velocities. doi:10.5194/se-2020-10

662 Anselmi, M., Govoni, A., De Gori, P., Chiarabba, C., 2011. Seismicity and velocity structures
663 along the south-Alpine thrust front of the Venetian Alps (NE-Italy). *Tectonophysics* 513,
664 37–48. doi:10.1016/j.tecto.2011.09.023

665 Bettinelli, P., Avouac, J.-P., Flouzat, M., Bollinger, L., Ramillien, G., Rajaure, S., Sapkota, S.,
666 2008. Seasonal variations of seismicity and geodetic strain in the Himalaya induced by
667 surface hydrology. *Earth and Planetary Science Letters* 266, 332–344.
668 doi:10.1016/j.epsl.2007.11.021

669 Borsa, A.A., Agnew, D.C., Cayan, D.R., 2014. Remote Hydrology. Ongoing drought-induced
670 uplift in the western United States. *Science* 345, 1587–1590.
671 doi:10.1126/science.1260279

672 Caporali, A., Braitenberg, C., Montone, P., Rossi, G., Valensise, G., Viganò, A., Zurutuza, J.,
673 2018. A quantitative approach to the loading rate of seismogenic sources in Italy.
674 *Geophys. J. Int.* 213, 2096–2111. doi:10.1093/gji/ggy112

675 Castellarin, A., Cantelli, L., 2000. Neo-Alpine evolution of the Southern Eastern Alps. *Journal*
676 *of Geodynamics* 30, 251–274. doi:10.1016/S0264-3707(99)00036-8

677 Chanard, K., Avouac, J.P., Ramillien, G., Genrich, J., 2014. Modeling deformation induced

678 by seasonal variations of continental water in the Himalaya region: Sensitivity to Earth
679 elastic structure. *J. Geophys. Res. Solid Earth* 119, 5097–5113.
680 doi:10.1002/2013JB010451

681 Chanard, K., Fleitout, L., Calais, E., Barbot, S., Avouac, J.-P., 2018. Constraints on transient
682 viscoelastic rheology of the asthenosphere from seasonal deformation. *Geophys. Res.*
683 *Lett.* 45, 2328–2338. doi:10.1002/2017GL076451

684 Chan, K., Lee, T.-W., Sejnowski, T.J., 2003. Variational Bayesian Learning of ICA with
685 Missing Data. *Neural Comput.* 15, 1991–2011. doi:10.1162/08997660360675116

686 Console, R., Jackson, D.D., Kagan, Y.Y., 2010. Using the ETAS model for catalog
687 declustering and seismic background assessment. *Pure appl. geophys.* 167, 819–830.
688 doi:10.1007/s00024-010-0065-5

689 Craig, T.J., Chanard, K., Calais, E., 2017. Hydrologically-driven crustal stresses and
690 seismicity in the New Madrid Seismic Zone. *Nat. Commun.* 8, 2143.
691 doi:10.1038/s41467-017-01696-w

692 D’Agostino, N., Silverii, F., Amoroso, O., Convertito, V., Fiorillo, F., Ventafriidda, G., Zollo, A.,
693 2018. Crustal deformation and seismicity modulated by groundwater recharge of karst
694 aquifers. *Geophys. Res. Lett.* 45, 12,253-12,262. doi:10.1029/2018GL079794

695 Danesi, S., Pondrelli, S., Salimbeni, S., Cavaliere, A., Serpelloni, E., Danecek, P., Lovati, S.,
696 Massa, M., 2015. Active deformation and seismicity in the Southern Alps (Italy): The
697 Montello hill as a case study. *Tectonophysics* 653, 95–108.
698 doi:10.1016/j.tecto.2015.03.028

699 Devoti, R., Riguzzi, F., Cinti, F.R., Ventura, G., 2018. Long-term strain oscillations related to
700 the hydrological interaction between aquifers in intra-mountain basins: A case study
701 from Apennines chain (Italy). *Earth and Planetary Science Letters* 501, 1–12.
702 doi:10.1016/j.epsl.2018.08.014

703 Devoti, R., Zuliani, D., Braitenberg, C., Fabris, P., Grillo, B., 2015. Hydrologically induced
704 slope deformations detected by GPS and clinometric surveys in the Cansiglio Plateau,
705 southern Alps. *Earth and Planetary Science Letters* 419, 134–142.
706 doi:10.1016/j.epsl.2015.03.023

707 Drouin, V., Heki, K., Sigmundsson, F., Hreinsdóttir, S., Ófeigsson, B.G., 2016. Constraints on
708 seasonal load variations and regional rigidity from continuous GPS measurements in
709 Iceland, 1997–2014. *Geophys. J. Int.* 205, 1843–1858. doi:10.1093/gji/ggw122

710 Famiglietti, J.S., Lo, M., Ho, S.L., Bethune, J., Anderson, K.J., Syed, T.H., Swenson, S.C., de
711 Linage, C.R., Rodell, M., 2011. Satellites measure recent rates of groundwater depletion
712 in California's Central Valley. *Geophys. Res. Lett.* 38. doi:10.1029/2010GL046442

713 Fantoni, R., Catellani, D., Merlini, S., Rogledi, S., Venturini, S., 2002. La registrazione degli
714 eventi deformativi cenozoici nell'avampese Veneto-Friulano. *Mem. Soc. Geol. It* 57,
715 301–313.

716 Faulkner, D.R., Jackson, C.A.L., Lunn, R.J., Schlische, R.W., Shipton, Z.K., Wibberley,
717 C.A.J., Withjack, M.O., 2010. A review of recent developments concerning the structure,
718 mechanics and fluid flow properties of fault zones. *Journal of Structural Geology* 32,
719 1557–1575. doi:10.1016/j.jsg.2010.06.009

720 Feng, J., Gu, K., 2017. Geomechanical Modeling of Stress and Fracture Distribution during
721 Contractional Fault-Related Folding. *GEP* 05, 61–93. doi:10.4236/gep.2017.511006

722 Filippini, M., Squarzoni, G., De Waele, J., Fiorucci, A., Vigna, B., Grillo, B., Riva, A., Rossetti,
723 S., Zini, L., Casagrande, G., Stumpp, C., Gargini, A., 2018. Differentiated spring
724 behavior under changing hydrological conditions in an alpine karst aquifer. *J Hydrol*
725 (Amst) 556, 572–584. doi:10.1016/j.jhydrol.2017.11.040

726 Fu, Y., Argus, D.F., Freymueller, J.T., Hefflin, M.B., 2013. Horizontal motion in elastic
727 response to seasonal loading of rain water in the Amazon Basin and monsoon water in
728 Southeast Asia observed by GPS and inferred from GRACE. *Geophys. Res. Lett.* 40,
729 6048–6053. doi:10.1002/2013GL058093

730 Galadini, F., Poli, M.E., Zanferrari, A., 2005. Seismogenic sources potentially responsible for
731 earthquakes with $M \geq 6$ in the eastern Southern Alps (Thiene-Udine sector, NE Italy).
732 *Geophys. J. Int.* 161, 739–762. doi:10.1111/j.1365-246X.2005.02571.x

733 Garcia-Aristizabal, A., 2018. Modelling fluid-induced seismicity rates associated with fluid
734 injections: examples related to fracture stimulations in geothermal areas. *Geophys. J.*
735 *Int.* 215, 471–493. doi:10.1093/gji/ggy284

736 Gegout, P., Boy, J.P., Hinderer, J., Ferhat, G., 2010. Modeling and Observation of Loading
737 Contribution to Time-Variable GPS Sites Positions, in: Mertikas, S.P. (Ed.), Gravity,
738 Geoid and Earth Observation: IAG Commission 2: Gravity Field, Chania, Crete, Greece,
739 23-27 June 2008, International Association of Geodesy Symposia. Springer Berlin
740 Heidelberg, Berlin, Heidelberg, pp. 651–659. doi:10.1007/978-3-642-10634-7_86

741 Gualandi, A., Nichele, C., Serpelloni, E., Chiaraluce, L., Anderlini, L., Latorre, D., Belardinelli,
742 M.E., Avouac, J.P., 2017a. Aseismic deformation associated with an earthquake swarm
743 in the northern Apennines (Italy). *Geophys. Res. Lett.* 44, 7706–7714.
744 doi:10.1002/2017GL073687

745 Gualandi, A., Perfettini, H., Radiguet, M., Cotte, N., Kostoglodov, V., 2017b. GPS
746 deformation related to the M 7.3, 2014, Papanao earthquake
747 (Mexico) reveals the aseismic behavior of the Guerrero seismic gap. *Geophys. Res.*
748 *Lett.* 44, 6039–6047. doi:10.1002/2017GL072913

749 Gualandi, A., Serpelloni, E., Belardinelli, M.E., 2016. Blind source separation problem in
750 GPS time series. *J. Geod.* 90, 323–341. doi:10.1007/s00190-015-0875-4

751 Hainzl, S., Aggarwal, S.K., Khan, P.K., Rastogi, B.K., 2014. Monsoon-induced earthquake
752 activity in Talala, Gujarat, India. *Geophys. J. Int.* 200, 627–637. doi:10.1093/gji/ggu421

753 Hainzl, S., Kraft, T., Wassermann, J., Igel, H., Schmedes, E., 2006. Evidence for rainfall-
754 triggered earthquake activity. *Geophys. Res. Lett.* 33. doi:10.1029/2006GL027642

755 Jensen, M.E., Burman, R.D., Allen, R.G., 1990. Evapotranspiration and irrigation water
756 requirements.

757 Johnson, C.W., Fu, Y., Bürgmann, R., 2017. Seasonal water storage, stress modulation, and
758 California seismicity. *Science* 356, 1161–1164. doi:10.1126/science.aak9547

759 Klimchouk, A.B., Sauro, U., 1996. Hidden shafts at the base of the epikarstic zone: a case
760 study from the Sette Comuni plateau, Venetian Pre-Alps, Italy. *Cave and karst science*
761 23, 101–107.

762 Lesparre, N., Boudin, F., Champollion, C., Chéry, J., Danquigny, C., Seat, H.C., Cattoen, M.,
763 Lizion, F., Longuevergne, L., 2017. New insights on fractures deformation from tiltmeter
764 data measured inside the Fontaine de Vaucluse karst system. *Geophys. J. Int.* 208,

765 1389–1402. doi:10.1093/gji/ggw446

766 Longuevergne, L., Florsch, N., Boudin, F., Oudin, L., Camerlynck, C., 2009. Tilt and strain
767 deformation induced by hydrologically active natural fractures: application to the
768 tiltmeters installed in Sainte-Croix-aux-Mines observatory (France). *Geophys. J. Int.*
769 178, 667–677. doi:10.1111/j.1365-246X.2009.04197.x

770 MacQueen, J., 1967. Some methods for classification and analysis of multivariate
771 observations. *Proceedings of the fifth Berkeley symposium on mathematical statistics*
772 *and probability* 1, 281–297.

773 Milanovic, P.T., 2005. *Water resources engineering in karst*.

774 Ogata, Y., 1998. Space-Time Point-Process Models for Earthquake Occurrences. *Ann. Inst.*
775 *Stat. Math.* 50, 379–402. doi:10.1023/A:1003403601725

776 Priolo, E., Romanelli, M., Plasencia Linares, M.P., Garbin, M., Peruzza, L., Romano, M.A.,
777 Marotta, P., Bernardi, P., Moratto, L., Zuliani, D., Fabris, P., 2015. Seismic monitoring of
778 an underground natural gas storage facility: the collalto seismic network. *Seismological*
779 *Research Letters* 86, 109–123. doi:10.1785/0220140087

780 Pushpalatha, R., Perrin, C., Le Moine, N., Mathevet, T., Andréassian, V., 2011. A downward
781 structural sensitivity analysis of hydrological models to improve low-flow simulation. *J*
782 *Hydrol (Amst)* 411, 66–76. doi:10.1016/j.jhydrol.2011.09.034

783 Rodell, M., Houser, P.R., Jambor, U., Gottschalck, J., Mitchell, K., Meng, C.J., Arsenault, K.,
784 Cosgrove, B., Radakovich, J., Bosilovich, M., Entin, J.K., Walker, J.P., Lohmann, D.,
785 Toll, D., 2004. The global land data assimilation system. *Bull. Amer. Meteor. Soc.* 85,
786 381–394. doi:10.1175/BAMS-85-3-381

787 Romano, M.A., Peruzza, L., Garbin, M., Priolo, E., Picotti, V., 2019. Microseismic Portrait of
788 the Montello Thrust (Southeastern Alps, Italy) from a Dense High-Quality Seismic
789 Network. *Seismological Research Letters*. doi:10.1785/0220180387

790 Rousseeuw, P.J., 1987. Silhouettes: A graphical aid to the interpretation and validation of
791 cluster analysis. *Journal of Computational and Applied Mathematics* 20, 53–65.
792 doi:10.1016/0377-0427(87)90125-7

793 Serpelloni, E., Pintori, F., Gualandi, A., Scoccimarro, E., Cavaliere, A., Anderlini, L.,

794 Belardinelli, M.E., Todesco, M., 2018. Hydrologically Induced Karst Deformation:
795 Insights From GPS Measurements in the Adria-Eurasia Plate Boundary Zone. *J.*
796 *Geophys. Res. Solid Earth* 123, 4413–4430. doi:10.1002/2017JB015252

797 Serpelloni, E., Vannucci, G., Anderlini, L., Bennett, R.A., 2016. Kinematics, seismotectonics
798 and seismic potential of the eastern sector of the European Alps from GPS and seismic
799 deformation data. *Tectonophysics* 688, 157–181. doi:10.1016/j.tecto.2016.09.026

800 Silverii, F., D’Agostino, N., Métois, M., Fiorillo, F., Ventafridda, G., 2016. Transient
801 deformation of karst aquifers due to seasonal and multiyear groundwater variations
802 observed by GPS in southern Apennines (Italy). *J. Geophys. Res. Solid Earth* 121,
803 8315–8337. doi:10.1002/2016JB013361

804 Torabi, A., Ellingsen, T.S.S., Johannessen, M.U., Alaei, B., Rotevatn, A., Chiarella, D., 2019.
805 Fault zone architecture and its scaling laws: where does the damage zone start and
806 stop? Geological Society, London, Special Publications SP496-2018–151.
807 doi:10.1144/SP496-2018-151

808 van Dam, T., Wahr, J., Milly, P.C.D., Shmakin, A.B., Blewitt, G., Lavallée, D., Larson, K.M.,
809 2001. Crustal displacements due to continental water loading. *Geophys. Res. Lett.* 28,
810 651–654. doi:10.1029/2000GL012120

811 Zhuang, J., Ogata, Y., Vere-Jones, D., 2002. Stochastic Declustering of Space-Time
812 Earthquake Occurrences. *J. Am. Stat. Assoc.* 97, 369–380.
813 doi:10.1198/016214502760046925